

Article

# Quasi-Equilibrium, Multifoil Platelets of Copper- and Titanium-Substituted Bismuth Vanadate, $\text{Bi}_2\text{V}_{0.9}(\text{Cu}_{0.1-x}\text{Ti}_x)\text{O}_{5.5-\delta}$ , by Molten Salt Synthesis

Kevin Ring and Paul Fuierer \*

Materials and Metallurgical Engineering Department, New Mexico Institute of Mining and Technology (New Mexico Tech), 801 LeRoy Place, Socorro, NM 87801, USA; kring@alumni.nmt.edu

\* Correspondence: paul.fuierer@nmt.edu; Tel.: +1-575-835-5497

Received: 11 March 2018; Accepted: 12 April 2018; Published: 17 April 2018



**Abstract:** 10% copper-substituted ( $\text{BiCuVOX}/\text{Bi}_2\text{V}_{0.9}\text{Cu}_{0.1}\text{O}_{5.5-\delta}$ ) and 5% copper/titanium double-substituted bismuth vanadate ( $\text{BiCuTiVOX}/\text{Bi}_2\text{V}_{0.9}(\text{Cu}_{0.05}\text{Ti}_{0.05})\text{O}_{5.5-\delta}$ ) platelets were formed by molten salt synthesis (MSS) using a eutectic KCl/NaCl salt mixture. The product was phase-pure within the limits of X-ray diffraction. The size and form of the platelets could be controlled by changing the heating temperature and time. The crystallite growth rate at a synthesis temperature of 650 °C and the activation energy for grain growth were determined for BICUTIVOX, which experienced inhibited growth compared to BICUVOX. Quasi-equilibrium, multifoil shapes consisting of lobes around the perimeter of the platelets were observed and explained in the context of relative two-dimensional nucleation and edge growth rates.

**Keywords:** bismuth vanadate; molten salt synthesis; platelet morphology; multifoil shape; Wulff shape; Ostwald ripening

## 1. Introduction

In 1988, Abraham et al. published the discovery of a new group of oxide ion-conducting ceramics based on bismuth vanadate ( $\text{Bi}_4\text{V}_2\text{O}_{11-\delta}$ ) [1]. This compound was determined to be a member of the Aurivillius family of crystal structures, and it was described as having alternating layers of  $(\text{Bi}_2\text{O}_2)^{2+}$  and  $(\text{VO}_{3.5}\square_{0.5})^{2-}$  [1]. Bismuth vanadate has three distinct phases, and from single crystal studies, the highest temperature  $\gamma$ -phase (normally occurring at  $T > 550$  °C) was determined to be tetragonal (space group  $I4/mmm$ ,  $a = 4.004$  Å,  $c = 15.488$  Å). Conductivity was found to be highly anisotropic; two orders of magnitude higher when perpendicular to the  $c$ -axis (in the  $a$ - $b$  plane) than parallel to the  $c$  axis [1–4]. It was later found that a partial substitution of an aliovalent metal cation for vanadium (first was copper at 10 mol %) resulted in the stabilization of the  $\gamma$ -phase at room temperature, and the term BIMEVOX was coined to refer to this and all subsequent formulations, where ME represents one of the many possible substitutive metal cations, typically a transition metal [2]. Having an oxide ion conductivity that is higher than any other ceramic (e.g., yttria-stabilized cubic zirconia ( $\text{Zr}_{1-x}\text{Y}_x\text{O}_{2-x/2}$  “YSZ”) at moderate temperatures, BIMEVOX compounds have generated interest over the years for their potential applications as solid oxide fuel cells, as oxygen separation pumps, as gas sensors [5–9], and very recently, as catalyst supports [10].

Just as with its conductivity, the anisotropy of the tetragonal phase is expected to result in anisotropy in the other chemical and physical tensor properties of BIMEVOX. While such differences are distinct in single crystals, a random polycrystalline sample exhibits an approximate average of the lattice-specific property coefficients. Enhancing the long-range texture of polycrystalline samples therefore holds promise for enhancing the desired properties of BIMEVOX ceramics; of chief interest

is maximizing the bidimensional ionic conductivity [11]. Experimental techniques for enhancing the texture of anisotropic ceramics have included pulsed laser deposition [12], magnetic or electric fields [13,14], and load-assisted sintering or “hot-forging” [14–16]. Shantha et al. [17], used a KCl flux in a two-stage, liquid-phase sintering process which resulted in densities of 97% and textures of up to 79% in BIMEVOX.

Another route for fabricating textured ceramics begins with particles already exhibiting the desired geometry and involves the use of these particles as seeds in “templated grain growth” (TGG). TGG has been used with reasonable success in conjunction with tape-casting for bismuth titanate ( $\text{Bi}_4\text{Ti}_3\text{O}_{12}$ ) and other layered perovskite-type compounds, achieving (001) textures exceeding 90% [18–23]. Due to the crystallographic anisotropy of bismuth titanate and other Aurivillius phases, the surface energy of the (001) planes is less than that of the (*hk*0) planes, and therefore, the growth of anisometric particles (i.e., platelets) is thermodynamically favorable; however, the kinetics in conventional, solid-state synthesis often limit such growth.

Molten salt synthesis (MSS), also called salt melt synthesis, is a favored method for producing such seed particles with a pronounced anisotropic growth; it involves reacting the material in a molten salt flux [24–29]. The molten salt acts as a diffusion-enhancing medium. Phase formation occurs by one of two mechanisms—solution–precipitation or solution–diffusion—depending on the relative solubility of the reactant species [27]. Grain growth by the Ostwald ripening of crystallites is controlled by two-dimensional (2D) nucleation and growth along a crystallographic vector through the generation of ledges on the propagating edge [27,30]. MSS has been used since the 1970s to synthesize binary and complex oxides using a variety of salt systems [24–27], but it is receiving renewed attention in the production of borides, carbides, silicides, and nanomaterials with high crystallinity [28,29]. MSS is high-temperature solution chemistry, but, compared to solid-state synthesis, allows for lower reaction temperatures and much faster mass transport by means of convection and diffusion through the liquid phase. The process is also attractive because it can be scaled up, and, depending on the salt system used, it can be economical and environmentally friendly through the recycling of water-soluble salts.

Roy and Fuierer [31] first published work on the successful synthesis of BICOVOX (cobalt-substituted bismuth vanadate) by MSS. Herein, we report for the first time the molten salt synthesis of BICUVOX and BICUTIVOX using similar techniques. The hypothesis is that the product of the solubility of oxide constituents,  $\text{Bi}_2\text{O}_3$ ,  $\text{V}_2\text{O}_5$ ,  $\text{CuO}$ , and  $\text{TiO}_2$ , is larger than the solubility of the compound  $\text{Bi}_4(\text{V}_{1-x-y}\text{Cu}_x\text{Ti}_y)_2\text{O}_{11-\delta}$ , leading to its formation under a high degree of supersaturation. Subsequent grain growth is expected to lead to highly anisometric particles. Furthermore, we investigate the influence of temperature, time, and double substitution (Cu plus Ti co-doping) on crystallite growth.

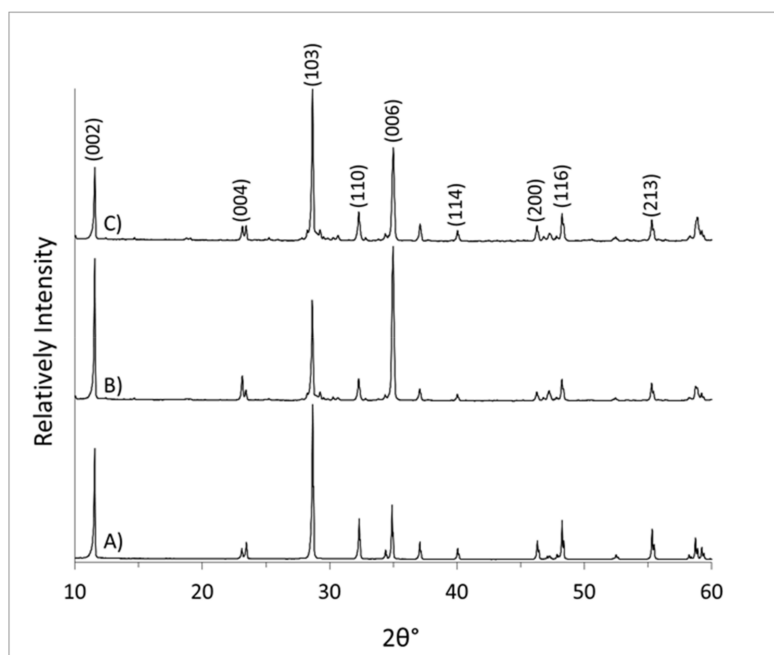
## 2. Materials and Methods

Stoichiometric amounts of bismuth (III) oxide (Alfa Aesar, 99%), vanadium (V) oxide (Acros Organics 99.6+%), titanium (IV) oxide (JT Baker, ACS grade), and copper (II) oxide (Aldrich, ACS grade) were combined with an equal mass of a eutectic ( $T_E = 640\text{--}657\text{ }^\circ\text{C}$  [32]) salt mixture comprised of a 0.506:0.494 molar ratio of sodium chloride (Fisher, 99+) and potassium chloride (Aldrich 99+). The batches were milled in a 250 mL, high-density polyethylene jar with 400 grams of 13 mm cylindrical, ceria-stabilized zirconia media, at approximately 130 rpm typically for 5 h. Milling was performed dry, and the media and powder were separated after milling using a #10 sieve (2 mm opening). Reactions were carried out in air using a Thermolyne 47900, a resistive wire heated muffle furnace. The material was placed in a covered alumina crucible and heated at a ramp rate of  $10\text{ }^\circ\text{C}/\text{min}$  to temperatures between  $610\text{ }^\circ\text{C}$  and  $700\text{ }^\circ\text{C}$ , and it was then held for 2–10 h. The net loss of mass after heat treatments never exceeded 0.5%. After heating, the charge of the product and the fused salt were broken up by soaking them in deionized water at  $\sim 75\text{ }^\circ\text{C}$  and then splitting them to expose the interior. The aggregated material was broken up and washed of the salt by stirring in 1.4 L of DI  $\text{H}_2\text{O}$  at  $60\text{ }^\circ\text{C}$  for periods of 30 min to 18 h. After the material settled, the water was decanted and replaced. This process was repeated a minimum of four times. The final product was oven-dried.

Powder samples for analysis were taken by stirring the entire yielded quantity and taking material from the center. XRD analysis was carried out with a PANalytical X'Pert Pro ( $\text{Cu}_{K\alpha}$  source, nickel filter, and a  $2.122^\circ$  X'Celerator line detector) over a  $2\theta$  of  $5.996^\circ$ – $70^\circ$ , with  $0.01671^\circ$  steps, and the data was analyzed with the accompanying HighScore Plus software. Patterns presented were modified from the raw scan data by dividing the intensity at each  $2\theta$  value in a set by the maximum intensity in that set (i.e., normalized to 1), and then those patterns were shifted by integer values to accommodate multiple patterns on the same chart. All patterns were indexed as  $I4/mmm$  tetragonal, according to ICDD PDF #01-070-9191 [33]. Microscopic analysis was performed using a Hitachi S-3200N scanning electron (SE) microscope. Crystallite platelet dimensions were measured using image digitization of SE micrographs. Particle size distribution analysis was performed by Fraunhofer laser (780 nm) diffraction using a Beckman Coulter LS 13 320, with the microliquid module filled with deionized water and loaded to 8–12% obscuration.

### 3. Results and Discussion

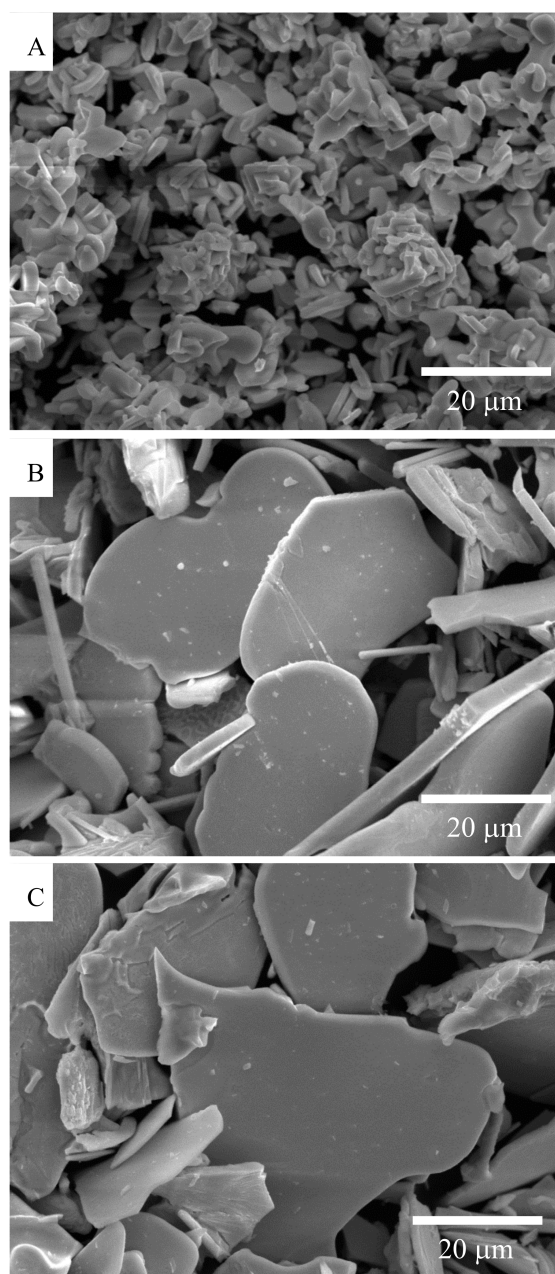
The series of XRD patterns for BICUVOX in Figure 1 shows that the  $\gamma$ -phase was successfully synthesized in all heat treatments and that no other phases were present within detectable limits. The enhanced ratio of  $(00l)/(013)$  peak intensities compared to the random powder pattern peak heights is an indication of an increase in population of  $c$ -axis-oriented platelets and their alignment under the mild shearing forces involved in the preparation of a powder sample for XRD analysis [34]. Comparing different temperatures, the sample synthesized at  $650^\circ\text{C}$  shows  $(00l)$  reflections of higher intensity than the material synthesized at  $610^\circ\text{C}$  and at  $675^\circ\text{C}$ . For the purposes of strong crystallite texturing, the result suggests that  $650^\circ\text{C}$  is the best temperature for synthesis.



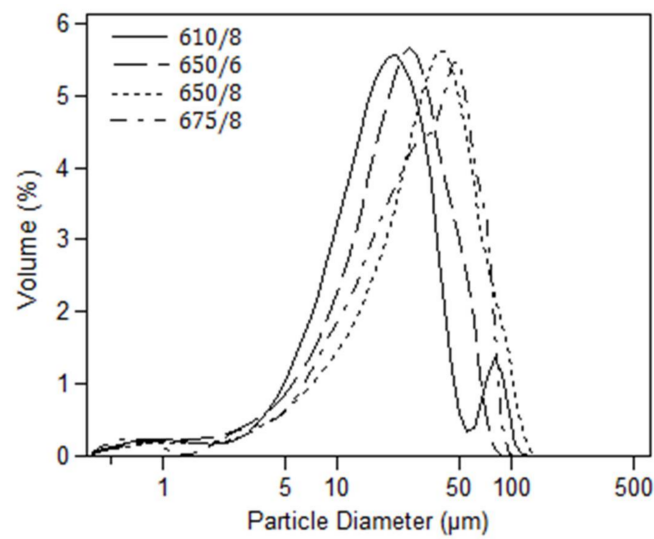
**Figure 1.** XRD pattern of BICUVOX platelets synthesized by molten salt synthesis (MSS): (A)  $610^\circ\text{C}/8\text{ h}$ , (B)  $650^\circ\text{C}/8\text{ h}$ , (C)  $675^\circ\text{C}/8\text{ h}$ .

Figure 2 shows SEM images of MSS BICUVOX. The  $610/8$  material appears to consist largely of agglomerates of small platelets. Although  $610^\circ\text{C}$  is substantially lower than the reported eutectic temperature of  $640$ – $657^\circ\text{C}$  [32], the solid salt still facilitates habit growth by enhancing the diffusion of ions [35]. With higher process temperatures and the presence of a fully molten salt, larger platelets result, with a majority of the faces having an irregular shape. An inspection of additional

micrographs suggests that the highest temperature (675 °C) also gives a greater population of smaller crystallites, resulting either from fracture or from larger platelets dissolving and re-nucleating as described [26,30,31]. An increase in population of broken and/or re-dissolved and nucleated particles is believed to be the cause of the decrease in (001) reflections for the 675 °C processed material. Figure 3 shows the distribution of particle sizes as measured by laser diffraction. As expected, the major mode shifts to a larger particle size with a process temperature and time, which is in general agreement with the SEM images. For the solid-salt synthesis at 610 °C, the small mode at a large size of about 80 microns is attributed to aggregation. For the 675 °C material, the shoulder located at about 30  $\mu\text{m}$  off of the major peak can be attributed to broken platelets.



**Figure 2.** SEM images of BICUVOX platelets formed by MSS at: (A) 610 °C/8 h, (B) 650 °C/8 h, (C) 675 °C/8 h.



**Figure 3.** Relative volume distribution of particle sizes for BICUVOX powders synthesized using salt matrix at various treatments  $T(^{\circ}\text{C})/t(\text{h})$ .

The diffraction patterns in Figure 4 show that the  $\gamma$ -phase for BICUTIVOX was also synthesized in all heat treatments. Again, all three patterns show higher  $(00l)/(103)$  intensity ratios than a random powder pattern [33]. In this case, there is a steady decrease in powder texture with an increasing synthesis temperature.

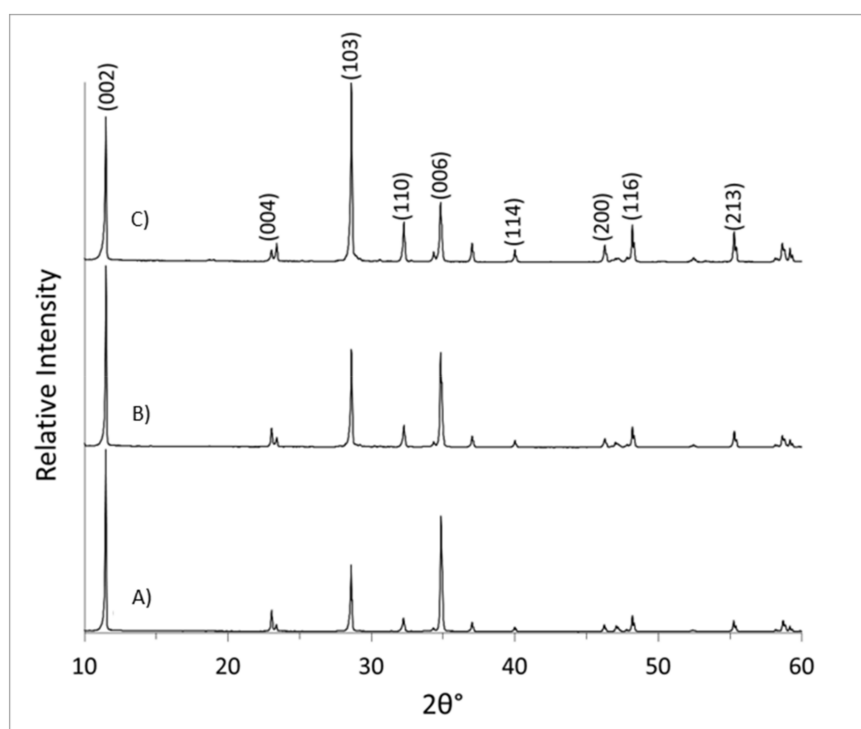


**Figure 4.** XRD pattern of BICUTIVOX platelets produced via MSS: (A)  $650^{\circ}\text{C}/8\text{ h}$ , (B)  $675^{\circ}\text{C}/8\text{ h}$ , (C)  $700^{\circ}\text{C}/8\text{ h}$ .

The SEM images in Figure 5 show populations of platelets, with some being quite rounded and others being irregular in geometry. The occurrence of platelets with edge lobes and multifoil shapes [36] is evident. A mechanistic explanation for the platelet shape and edge lobes is proposed

later in the study. The size of the platelets shows a steady increase with the process temperature. Figure 6 shows the size distribution of particles by laser diffraction, and it also shows the major peak shifting to a smaller size with an increasing temperature. This is contrary to what is expected when compared to the result for BICUVOX, and it is not in agreement with the impression obtained from the SEM micrographs. See Figure 7 for a larger perspective view and also a direct comparison of BICUVOX and BICUTIVOX at equivalent process conditions.

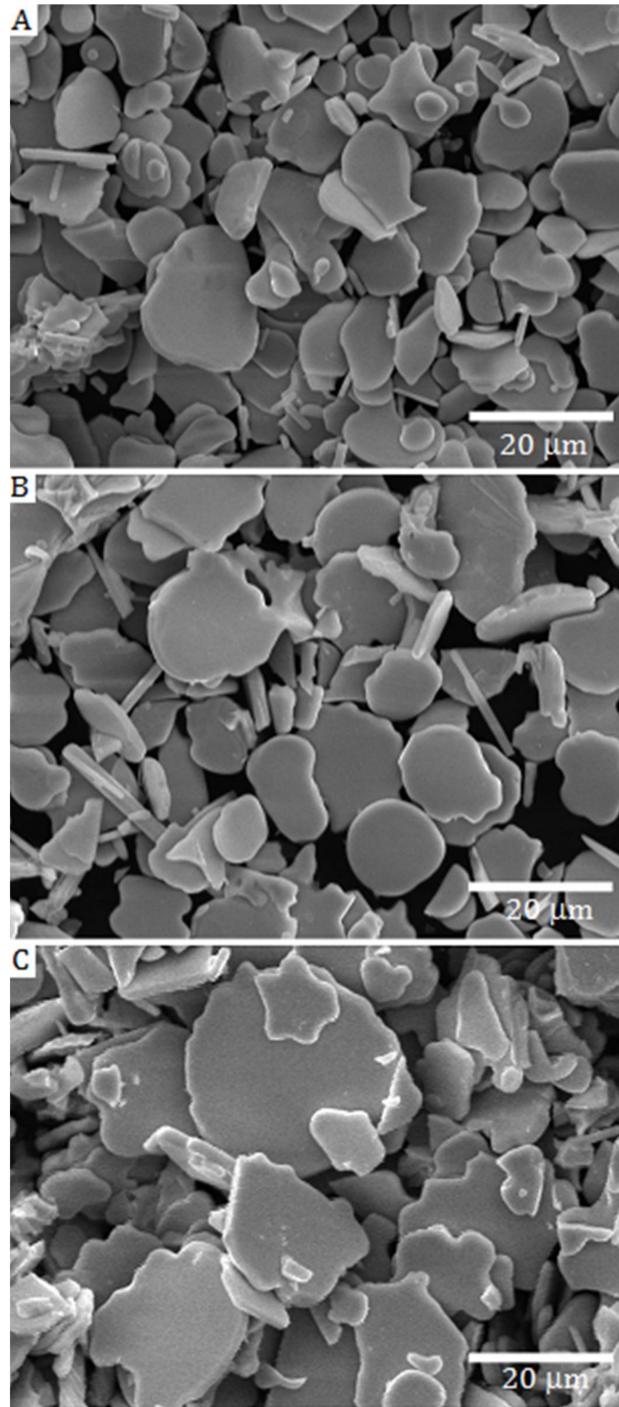


**Figure 5.** SEM images of BICUTIVOX platelets formed by MSS at: (A) 650 °C/8 h, (B) 675 °C/8 h, (C) 700 °C/8 h.

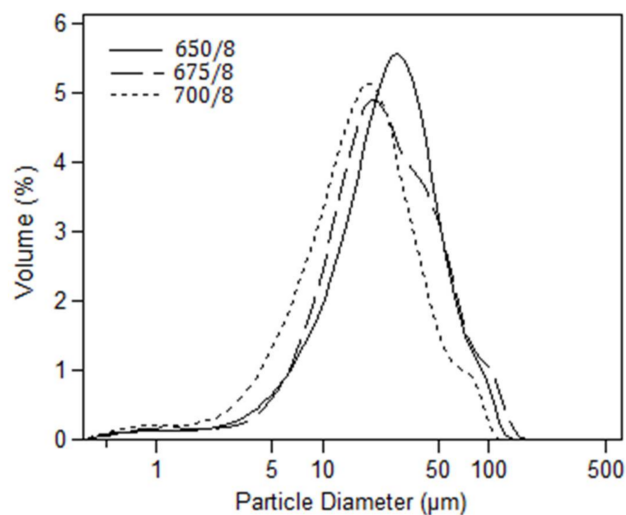


**Figure 6.** Relative volume distribution of particle sizes for BICUTIVOX platelets synthesized using molten salt at various treatments T(°C)/t(h).

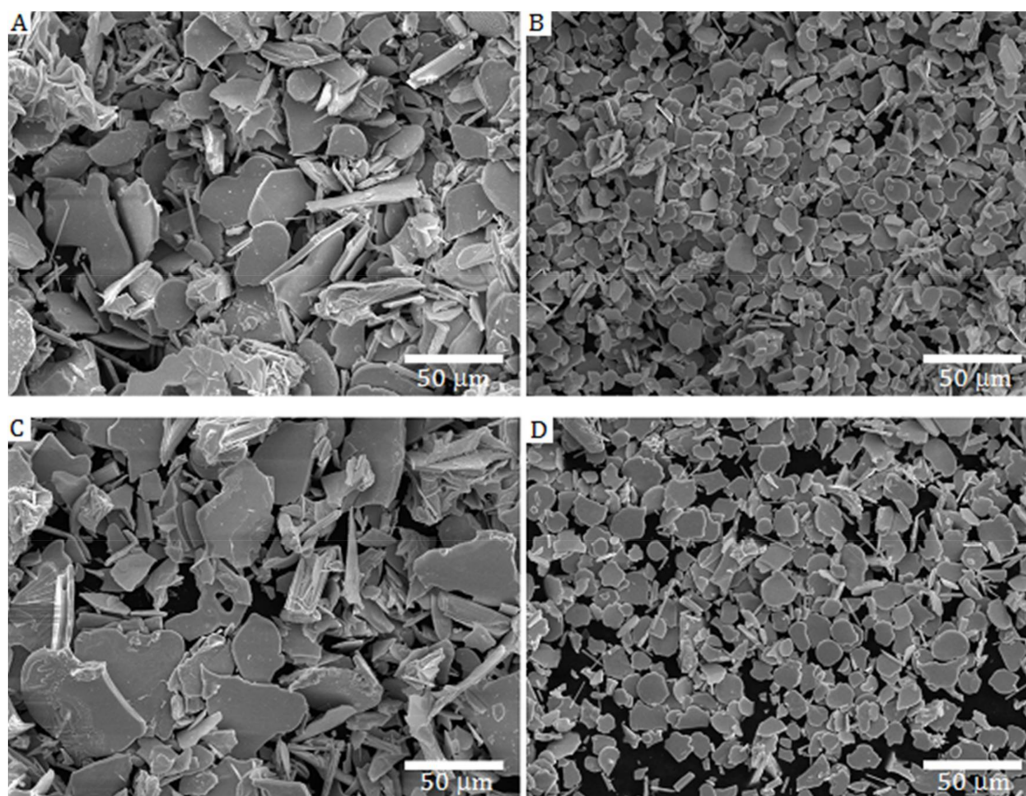


**Figure 7.** SEM images of BICUVOX (left) and BICUTIVOX (right) synthesized under the same conditions: (A) BICUVOX, 650 °C/8 h, (B) BICUTIVOX, 650 °C/8 h, (C) BICUVOX, 675 °C/8 h, (D) BICUTIVOX, 675 °C/8 h.

Particle sizing by laser diffraction is challenging for platelet-type particles and can be misleading because the technique assumes an equivalent spherical diameter, and is subject to the influence of fractured particles and agglomeration. Hence, a direct approach was adopted using SEM images for a more accurate particle size measurement and analytics. Four representative micrographs from each sample, with particles well-dispersed on carbon tape, were carefully analyzed. Dimensions were

taken of any particle whose large face was oriented normal to the viewing axis. Platelets which were obviously fractured were not used. Likewise, all edge-on particles were used to measure platelet thickness. Statistical values of these populations ( $N > 100$ ) of particles are summarized in Table 1. Despite the rather large standard deviations in some samples, the table shows a general trend of increased average and maximum platelet sizes with increasing temperatures. At a fixed process temperature of 650 °C, a steady increase in average size with time is apparent. The aspect ratio (AR) undergoes little change except from solid to molten salt (i.e., 610 °C vs. 650 °C). Also given in Table 1 are Lotgering Orientation factors,  $F$ , obtained from the XRD patterns in Figures 1 and 4, calculated by [37]:

$$F = \frac{p - p_0}{1 - p_0} \quad \text{and} \quad p = \frac{\sum I(00l)}{\sum I(hkl)} \quad (1)$$

where  $p$  is equal to the sum of the intensities of the selected family of planes divided by the sum of the intensities for all planes within the pattern;  $p_0$  is the factor for a non-textured sample (randomly oriented powder pattern [33]). This is a relative measure of the number and tendency for the orientation of  $c$ -axis platelets in the packed powder XRD samples. The  $F$  factor is highest for a process temperature of 650 °C for both materials. Platelet breakage, dissolution/nucleation, and increased edge roughness are all believed to be responsible for the decrease in powder XRD texture with a higher process temperature.

**Table 1.** Dimensional statistics and orientation factor,  $F$ , of salt-synthesized BIMEVOX platelets.

Phase	Treatment	$F_{(001)}$	$D_{ave} \pm D_{StDev}$	$D_{max}$	$AR \pm AR_{StDev}$
	T(°C)/t(h)	( $\mu\text{m}$ )	( $\mu\text{m}$ )		
BICUVOX	610/8	0.14	$7.2 \pm 1.5$	11.7	$8 \pm 3$
	650/2		$24.5 \pm 2.0$	36.3	$13 \pm 3$
	650/4		$27.0 \pm 4.5$	47.5	$13 \pm 3$
	650/6	0.33	$26.9 \pm 7.2$	35.1	$12 \pm 3$
	650/8	0.43	$33.5 \pm 10.3$	49.4	$15 \pm 8$
	650/10		$29.1 \pm 5.5$	44.9	$9 \pm 2$
	675/8	0.23	$37.3 \pm 21.1$	65.5	$15 \pm 9$
BICUTIVOX	650/2		$9.6 \pm 0.6$	12.9	$8 \pm 3$
	650/4		$11.0 \pm 3.2$	21.7	$11 \pm 3$
	650/6		$13.6 \pm 0.5$	18.3	$9 \pm 2$
	650/8	0.6	$16.1 \pm 2.7$	29.2	$10 \pm 2$
	650/10		$16.3 \pm 3.0$	24.3	$7 \pm 1$
	675/8	0.47	$17.9 \pm 2.8$	25.0	$11 \pm 3$
	700/8	0.22	$21.3 \pm 4.2$	32.1	$10 \pm 3$

Particle growth can be represented by the following equation [38–40]:

$$D^2 - D_0^2 = k(t - t_0) \exp\left(-\frac{E_a}{RT}\right) \quad (2)$$

where  $D$  is the average particle size at time  $t$ ,  $D_0$  is the initial particle size at initial time  $t_0$ ,  $k$  is the rate constant,  $E_a$  is the activation energy for particle growth,  $R$  is the gas constant, and  $T$  is the synthesis temperature. Figure 8 shows a plot of  $2\ln(D)$  vs inverse temperature for the two compositions. From the slope of the best fit line, an activation energy of 83 kJ/mol for particle growth for BICUTIVOX is estimated. This value is between 32 kJ/mol for  $\text{BaBi}_4\text{Ti}_4\text{O}_{15}$  (another Aurivilius-type phase) synthesized in  $\text{K}_2\text{SO}_4$ – $\text{Na}_2\text{SO}_4$  flux [40], and 96 kJ/mol for  $\text{Pb}(\text{Mg}_{0.33}\text{Nb}_{0.67})\text{O}_3$  (perovskite) in  $\text{Li}_2\text{SO}_4$ – $\text{Na}_2\text{SO}_4$  flux [38], and this value is considered reasonably accurate. With only two molten salt data points and larger deviation for BICUVOX, the activation energy cannot be calculated, but it appears to be lower than for BICUTIVOX. Also plotted on the graph is the single data point for the solid-salt-synthesized BICUVOX, which falls far below the other data points due to a different limiting mechanism for growth in the solid state below the NaCl–KCl eutectic temperature.

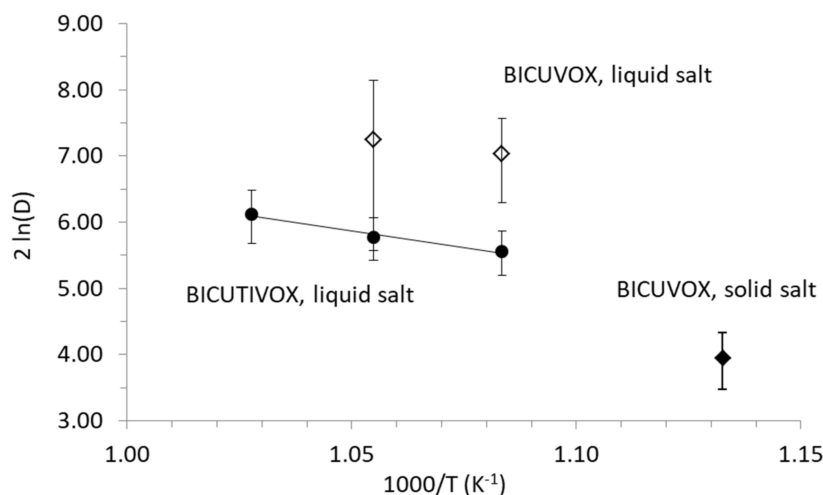


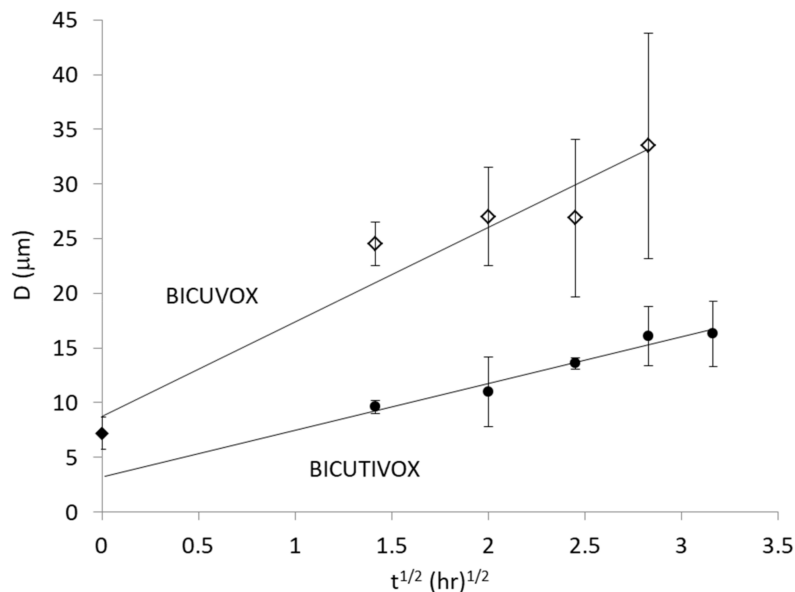
**Figure 8.** Plot of  $2\ln(D)$  ( $D$  = platelet diameter) versus inverse temperature for salt-synthesized BICUVOX and BICUTIVOX according to the particle growth model. Error bars show  $\pm$  one  $D_{stddev}$ .

According to Equation (2) and the well-known parabolic rate law, the platelet diameter,  $D$ , is plotted against the square root of time for a process temperature of 650 °C (Figure 9). BICUTIVOX data appear to be well-behaved. Using the activation energy for growth (83 kJ/mol) in Equation (2) and the slope of the best fit line, one obtains a grain growth rate constant of  $9.6 \times 10^{-16}$  cm<sup>2</sup>/s. In this case, the  $y$ -intercept is 3.2  $\mu$ m (interpreted as the starting grain size,  $D_0$ ). If the best fit line is forced through the origin (starting size  $D_0 = 0$   $\mu$ m), then the rate constant increases to  $16 \times 10^{-16}$  cm<sup>2</sup>/s. This rate constant is far below the estimated mobility of ionic species in a molten salt ( $1 \times 10^{-8}$  cm<sup>2</sup>/s), but is not far from the estimated mobility of species in the solid state ( $1 \times 10^{-18}$  cm<sup>2</sup>/s [18]). This suggests that the limiting mechanism for grain growth is the diffusion at the surface or near the surface of the platelets. For BICUVOX, the data is less well-behaved, falling further off the best fit line. This is due to the significantly larger standard deviation in the particle size data, due in part to excessive breakage as the maximum platelet size approaches 50  $\mu$ m (see Table 1). The 650 °C/6 h statistics suggest that this sample in particular was affected. Note that the experimental grain size from the solid salt synthesis is used as the non-zero starting grain size,  $D_0$ , which can be justified because BICUVOX formation took place prior to the existence of the liquid salt. Although we do not calculate a value for the growth rate constant due to the absence of a calculated activation energy, the rate constant appears to be larger for BICUVOX than for BICUTIVOX.

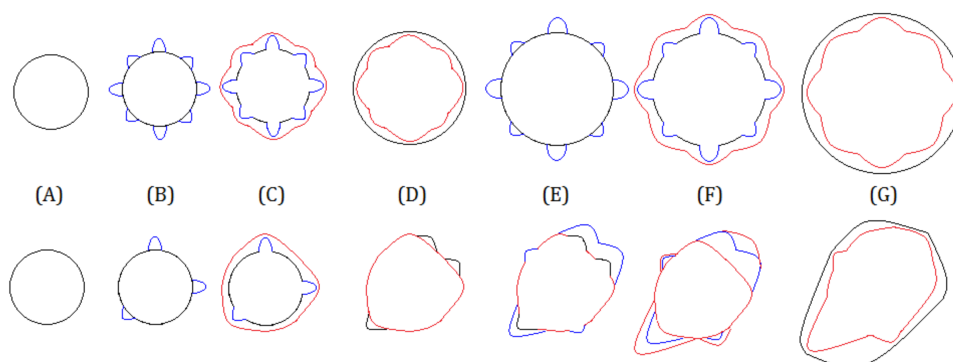
An inspection of the micrographs (Figures 2, 5 and 7) reveals the differences between BICUVOX and BICUTIVOX. The most obvious difference is the size difference, but there is also a difference in particle form and edge angularity. BICUTIVOX particles can be described as having a discoidal form with a high circularity, and being sub-angular to well-rounded. In some cases, the particle takes on a multifoil shape reminiscent of a Wulff construction [41–43]. Note the small pentafoil star on top of the larger, nearly round, multifoil platelet in Figure 5B. BICUVOX, on the other hand, can be described as discoidal with a low circularity, and having angular to sub-rounded edges.

Figure 10 is a schematic which aids the description of the platelet growth and provides an explanation for their quasi-equilibrium, multifoil shapes. The top row represents BICUTIVOX. The bottom row represents BICUVOX. In general, particles of Aurivillius-type, bismuth, layered-structure compounds are expected to have atomically smooth ( $00l$ ) faces and atomically rough ( $hk0$ ) faces [44], so high surface area sites nucleate along the propagating edge of a platelet (Figure 10B). During Ostwald ripening, a kinetic restriction (surface diffusion) regulates the growth of the platelets but does not affect the 2D-nucleation rates for the ledge generation. In BICUTIVOX, nucleation of ledges (with fast kinetics) is distributed evenly about the perimeter of the crystallite, and so, the growth of the propagating edge happens evenly in all directions (Figure 10C). The nucleation–growth

process repeats itself as the particle grows (Figure 10D–G). For some particles, the process is interrupted at the nucleation stage while others are interrupted at the edge growth stage or somewhere in-between (see especially Figure 5B). The lobes are more pronounced and more numerous in the higher temperature (700 °C) material because the rate of nucleation is very high. In the case of BICUVOX, the mechanism of platelet growth is the same, except that there is a difference in the speed of edge propagation because the rate constant is higher (as seen in Figure 9). In BICUVOX, soon after the nucleation of a ledge site, the edge begins to grow around it as the cusp fills in due to capillary pressure. Because this growth step happens more rapidly than in BICUTIVOX, the growth does not occur evenly in all directions; thus, this leads to the lack of circularity in BICUVOX platelets.



**Figure 9.** Platelet diameter versus the square root of time plots for BICUVOX and BICUTIVOX at an MSS process temperature of 650 °C. Exception: The solid point at  $t = 0$  is the experimental grain size of BICUVOX measured from solid salt synthesis at 610 °C, and it is taken as an approximation of the starting grain size (error bars show  $\pm$  one  $D_{stddev}$ ).



**Figure 10.** Schematic description of the kinetically limited growth mechanism undergone by BICUTIVOX (**upper row**) as compared to BICUVOX (**bottom row**). Different colors are used to indicate sequential layers of nucleation–growth.

The presence of the  $Ti^{4+}$  likely does not have a large effect on molten-salt-liquid-diffusion rates, but it noticeably increases the activation energy and decreases the rate constant for growth. This is consistent with the known effect of solid solution, aliovalent impurities, or substitutions acting as grain growth inhibitors in ceramics [39,45]. In the presence of such solute ions, the activation energy

for boundary migration is the sum of the vacancy migration, vacancy creation, impurity solution, and strain energy terms, but it is difficult to separate the relative contribution of each factor. Since doped BICUVOX contains significant oxygen vacancies and is a fast oxide ion conductor particularly in the  $a$ - $b$  plane, it is conceivable that cations are the rate-limiting diffusing species.

While evidence of edge roughness and lobes on MSS platelets can be found in previous published works [25,46,47], they generally do not appear as pronounced or as regular multifoil shapes like the BICUTIVOX material presented here. The closest example is found in Nd/V co-doped  $\text{Bi}_4\text{Ti}_3\text{O}_{12}$  by Tang et al. [47]. To our knowledge, the shapes have not been explained or even addressed. The BICUTIVOX multifoil and lobed platelets synthesized in this work are similar to Wulff-construction polar plots of the anisotropic surface energies of crystal planes. They can be described as quasi-equilibrium shapes which result from the combination of both surface energy anisotropy and growth rate anisotropy, not just between  $(00l)$  and  $(hk0)$  planes, but also within the family of  $(hk0)$  planes. The growth rate anisotropy occurs when a particular crystal face affords easy atom/ion attachment and grows rapidly, and it can result in shapes which exaggerate actual surface energy anisotropies [48]. The identification of the crystal planes within a multifoil platelet, their correlation with edge lobes, and the role of aliovalent dopants are the subjects of future work.

#### 4. Conclusions

The  $\gamma$ -phase of both BICUVOX and BICUTIVOX can be synthesized from simple metal oxides using a NaCl–KCl eutectic mix in an MSS process. The salt flux enhances grain growth with platelet habit, even with a process temperature that is 40 °C below the eutectic temperature, indicating that whether solid or liquid, the salt increases the diffusion rates of ions and facilitates anisotropic growth. The average size of platelets increases with the process temperature as expected, but when the platelets grow to a diameter in excess of about 50  $\mu\text{m}$ , significant fracturing can be expected due to the rigors of post-processing (washing/filtering), and therefore, there is a practical limit to how large the platelets can be synthesized and recovered. Optimal results with respect to achieving high grain ( $c$ -axis or  $(00l)$ ) orientation factors are achieved at 650 °C—very near the salt eutectic temperature—for both compounds.

Titanium ions,  $\text{Ti}^{4+}$ , as a second, aliovalent substitution for  $\text{V}^{5+}$ , acts as a particle growth inhibitor during MSS. The activation energy for platelet growth of BICUTIVOX in the molten salt is estimated to be 83 kJ/mol, which is consistent with MSS values reported in the literature for other simple and complex perovskites. The (growth) reaction rate constant at 650 °C is estimated to be  $1.0 \times 10^{-15} \text{ cm}^2/\text{s}$ , indicating that the limiting mechanism for platelet growth is the (near) surface reaction and diffusion. Excessive breakage of large platelets of BICUVOX causes greater uncertainty in particle size measurement, and precludes the calculation of grain growth activation energy and rate constant, but evidence suggests that these are lower and higher, respectively, than for BICUTIVOX. Due to the significant difference in 2D nucleation and edge propagation rates during Ostwald ripening, BICUTIVOX shows a tendency for multifoil platelet shapes with pronounced lobes extending from platelet edges. Faster volume and/or surface diffusion in BICUVOX allows for a higher overall growth rate and causes the platelet shape to be noncircular and more angular. Future interest may lie in producing lobed platelets with a higher surface area to take advantage of the high oxide ion mobility in the  $(00l)$  ( $a$ - $b$  crystal) plane and the functionality of the  $(hk0)$  surfaces in BICUTIVOX.

**Acknowledgments:** This research was funded by the National Science Foundation (Materials World Network, Division of Materials Research grant # 1108466). The authors also acknowledge the assistance of Riley Reprogge with image analysis and particle size measurement.

**Author Contributions:** Kevin Ring performed the synthesis and characterization of the samples, and wrote the first draft of the manuscript. Paul Fuierer conceived the original idea, managed the overall project, and wrote and edited the final manuscript.

**Conflicts of Interest:** The authors declare no conflict of interest.

## References

1. Abraham, K.; Debreuille, M.; Mairesse, G.; Nowogrocki, G. Phase transitions and ionic conductivity in  $\text{Bi}_4\text{V}_2\text{O}_{11}$  an oxide with a layered structure. *Solid State Ion.* **1988**, *28–30*, 529–532. [[CrossRef](#)]
2. Abraham, F.; Boivin, J.; Mairesse, G.; Nowogrocki, G. The BIMEVOX Series: A New Family of High Performance Oxide Ion Conductors. *Solid State Ion.* **1990**, *40–41*, 934–937. [[CrossRef](#)]
3. Yaremchenko, A.; Avdeev, M.; Kharton, K.; Kovalevsky, A.; Naumovich, E.; Marques, F. Structure and electronic conductivity of  $\text{Bi}_{2-x}\text{La}_x\text{V}_{0.9}\text{Cu}_{0.1}\text{O}_{5.5-\delta}$ . *Mater. Chem. Phys.* **2002**, *77*, 552–558. [[CrossRef](#)]
4. Kurek, P.; Dygas, J.; Breiter, M. Impedance measurements on single crystals of the oxygen ion conductor BICUVOX. *J. Electroanal. Chem.* **1994**, *378*, 77–83. [[CrossRef](#)]
5. Goodenough, J. Oxide-Ion Electrolytes, a review. *Ann. Rev. Mater. Res.* **2003**, *33*, 91–128. [[CrossRef](#)]
6. Kendall, K.; Navas, C.; Thomas, J.; Loye, H. Recent Developments in Oxide Ion Conductors: Aurivillius Phases. *Chem. Mater.* **1996**, *8*, 642–649. [[CrossRef](#)]
7. Cho, H.; Sakai, G.; Shimano, K.; Yamazoe, N. Preparation of BiMeVOx (Me=Cu, Ti, Zr, Nb, Ta) compounds as solid electrolyte and behavior of their oxygen concentration cells. *Sens. Actuators B Chem.* **2005**, *109*, 307–314. [[CrossRef](#)]
8. Kida, T.; Minami, T.; Kishi, S.; Yuasa, M.; Shimano, K.; Yamazoe, N. Planar-type BiCuVOx solid electrolyte sensor for the detection of volatile organic compounds. *Sens. Actuators B Chem.* **2009**, *137*, 147–153. [[CrossRef](#)]
9. Kida, T.; Harano, H.; Minami, T.; Kishi, S.; Morinaga, N.; Yamazoe, N.; Shimano, K. Control of electrode reactions in a mixed-potential-type gas sensor based on a BiCuVOx solid electrolyte. *J. Phys. Chem. C* **2010**, *114*, 15141–15148. [[CrossRef](#)]
10. Patil, B.; Sharma, S.; Mohanta, H.; Roy, B. BINIVOX catalyst for hydrogen production from ethanol by low temperature steam reforming (LTSR). *J. Chem. Sci.* **2017**, *129*, 1741–1746. [[CrossRef](#)]
11. Fuierer, P.; Maier, R.; Roder-Roith, U.; Moos, R. Processing Issues Related to the Bi-dimensional Ionic Conductivity of BIMEVOX Ceramics. *J. Mater. Sci.* **2011**, *46*, 5447–5453. [[CrossRef](#)]
12. Sant, C.; Contour, J. Pulsed laser deposition of  $\text{Bi}_4\text{Cu}_{2x}\text{V}_{2(1-x)}\text{O}_{11}$  thin films. *J. Cryst. Growth* **1995**, *153*, 63–67. [[CrossRef](#)]
13. Muller, C.; Chateigner, D.; Anne, M.; Bacmann, M.; Fouletier, J.; Rango, P. Pressure and magnetic field effects on the crystallographic texture and electrical conductivity of the compound. *J. Phys. D Appl. Phys.* **1996**, *29*, 3106–3111. [[CrossRef](#)]
14. Fuierer, P.; Nichtawitz, A. Electric Field Assisted Hot Forging of Bismuth Titanate. In Proceedings of the IEEE International Symposium on Applications of Ferroelectrics, University Park, PA, USA, 7–10 August 1994; pp. 126–129.
15. Fuierer, P.; Newnham, R. Newnham,  $\text{La}_2\text{Ti}_2\text{O}_7$  Ceramics. *J. Am. Ceram. Soc.* **1991**, *74*, 2876–2881. [[CrossRef](#)]
16. Fuierer, P.; Maier, M.; Exner, J.; Moos, R. Anisotropy and thermal stability of hot-forged BICUTIVOX oxygen ion conducting ceramics. *J. Eur. Ceram. Soc.* **2014**, *34*, 943–951. [[CrossRef](#)]
17. Shantha, K.; Varma, K. Fabrication and characterization of grain-oriented bismuth vanadate ceramics. *Mater. Res. Bull.* **1997**, *32*, 1581–1591. [[CrossRef](#)]
18. Seth, V.; Schulze, W. Grain-Oriented Fabrication of Bismuth Titanate Ceramics and Its Electrical Properties. *IEEE Trans. Ultrason. Ferroelectr. Freq. Control* **1989**, *36*, 41–42. [[CrossRef](#)] [[PubMed](#)]
19. Watanabe, H.; Kimura, T.; Yamaguchi, T. Particle Orientation during Tape Casting in the Fabrication of Grain-Oriented Bismuth Titanate. *J. Am. Ceram. Soc.* **1989**, *72*, 289–293. [[CrossRef](#)]
20. Horn, J.; Zhang, S.; Selvaraj, U.; Messing, G.; Trolier, S. Templated Grain Growth of Textured Bismuth Titanate. *J. Am. Ceram. Soc.* **1999**, *82*, 921–926. [[CrossRef](#)]
21. Yilmaz, H.; Messing, G.; Trolier, S. (Reactive) Templated Grain Growth of Textured Sodium Bismuth Titanate ( $\text{Na}_{0.5}\text{Bi}_{0.5}\text{TiO}_3$ - $\text{BaTiO}_3$ ) Ceramics-I Processing. *J. Electroceram.* **2003**, *11*, 207–215. [[CrossRef](#)]
22. West, D.; Payne, D. Reactive-Templated Grain Growth of  $\text{Bi}_{0.5}(\text{Na,K})_{0.5}\text{TiO}_3$ : Effects of Formulation on Texture Development. *J. Am. Ceram. Soc.* **2003**, *86*, 1132–1137. [[CrossRef](#)]
23. Kimura, T.; Yoshida, Y. Origin of Texture Development in Barium Bismuth Titanate Prepared by the Templated Grain Growth Method. *J. Am. Ceram. Soc.* **2006**, *89*, 869–874. [[CrossRef](#)]
24. Arendt, R.; Rosolowski, J.; Szymaszek, J. Lead zirconate titanate ceramics from molten salt solvent synthesized powders. *Mater. Res. Bull.* **1979**, *15*, 703–709. [[CrossRef](#)]
25. Kimura, T.; Yamaguchi, T. Fused Salt Synthesis of  $\text{Bi}_4\text{Ti}_3\text{O}_{12}$ . *Ceram. Int.* **1983**, *9*, 13–17. [[CrossRef](#)]

26. Li, Z.; Zhang, X.; Hou, J.; Zhou, K. Molten salt synthesis of anisometric  $\text{Sr}_3\text{Ti}_2\text{O}_7$  particles. *J. Cryst. Growth* **2007**, *305*, 265–270. [[CrossRef](#)]
27. Kimura, T. Chapter 4. Molten Salt Synthesis of Ceramic Powders. In *Advances in Ceramics—Synthesis and Characterization, Processing and Specific Applications*; Sikalidis, C., Ed.; INTECH: Rijeka, Croatia, 2011; pp. 75–100, ISBN 978-953-307-505-1.
28. Liu, X.; Fechler, N.; Antonietti, M. Salt melt synthesis of ceramics, semiconductors and carbon nanostructures. *Chem. Soc. Rev.* **2013**, *42*, 8237–8265. [[CrossRef](#)] [[PubMed](#)]
29. Preethi, G.; Ninan, A.; Kumar, K.; Balan, R.; Nagaswarupa, H. Molten Salt Synthesis of Nanocrystalline  $\text{ZnFe}_2\text{O}_4$  and Its Photocatalytic Dye Degradation Studies. *Mater. Today Proc.* **2017**, *4*, 11816–11819. [[CrossRef](#)]
30. Kang, M.; Kim, D.; Hwang, N. Ostwald ripening kinetics of angular grains dispersed in a liquid phase by two dimensional nucleation and abnormal grain growth. *J. Eur. Ceram. Soc.* **2002**, *22*, 603–612. [[CrossRef](#)]
31. Roy, B.; Fuierer, P. Molten Salt Synthesis of  $\text{Bi}_4(\text{V}_{0.85}\text{Co}_{0.15})_2\text{O}_{11-\delta}$  (BICOVOX) Ceramic Powders. *J. Am. Ceram. Soc.* **2009**, *92*, 520–523. [[CrossRef](#)]
32. Sangster, J.; Pelton, A. Phase Diagrams and Thermodynamic Properties of the 70 Binary Alkali Halide Systems Having Common Ions. *J. Phys. Chem. Ref. Data* **1987**, *16*, 509. [[CrossRef](#)]
33. International Center for Diffraction Data. Powder Diffraction File #01-070-9191, Bismuth Vanadium Copper Oxide; International Center for Diffraction Data: Newtown Square, PA, USA.
34. Inoue, M.; Hirasawa, I. The relationship between crystal morphology and XRD peak intensity on  $\text{CaSO}_4 \cdot 2\text{H}_2\text{O}$ . *J. Cryst. Growth* **2013**, *380*, 169–175. [[CrossRef](#)]
35. Roy, B.; Scott, P.; Ahrenkiel, Y.; Fuierer, P. Controlling the Size and Morphology of  $\text{TiO}_2$  Powder by Molten and Solid Salt Synthesis. *J. Am. Ceram. Soc.* **2008**, *91*, 2455–2463. [[CrossRef](#)]
36. Betz, W.; Webb, H. *Plane Geometry, Book, V. Regular Polygons and Circles*; Ginn & Co.: Cambridge, UK, 1921; p. 321.
37. Lotgering, F. Topotactical Reaction with Ferrimagnetic Oxides Having Hexagonal Structures. *J. Inorg. Nucl. Chem.* **1959**, *9*, 113–123. [[CrossRef](#)]
38. Yoon, K.; Yong, S.; Kang, D. Review: Molten Salt synthesis of lead-based relaxors. *J. Mater. Sci.* **1998**, *33*, 2977–2984. [[CrossRef](#)]
39. Kapadia, L. *The Mechanism of Grain Growth in Ceramics*; NASA Report; NASA: Washington, DC, USA, 1973; pp. 6–34.
40. Gu, Y.; Huang, J.; Li, L.; Zhang, K.; Wang, X.; Li, Q.; Tan, X.; Xu, H. Molten salt synthesis of anisotropy  $\text{BaBi}_4\text{Ti}_4\text{O}_{15}$  powders in  $\text{K}_2\text{SO}_4\text{-Na}_2\text{SO}_4$  flux. *Mater. Sci. Forum* **2011**, *687*, 333–338. [[CrossRef](#)]
41. Wulff, G. Zur Frage der Geschwindigkeit des Wachstums und der Auflösung der Krystallflächen. *Z. Kristallogr.* **1901**, *34*, 449–530. [[CrossRef](#)]
42. Herring, C. Some Theorems on the Free Energies of Crystal Surfaces. *Phys Rev.* **1951**, *82*, 87–93. [[CrossRef](#)]
43. Kang, S.C. 15 Grain Shape and Grain Growth in a Liquid Matrix. In *Sintering*; Elsevier: London, UK, 2005; p. 218.
44. Kimura, T.; Tani, T. Chapt 15, Processing and Properties of Textured Bismuth Layer-Structured Ferroelectrics. In *Lead Free Piezoelectrics*; Priya, S., Nahm, S., Eds.; Springer: New York, NY, USA, 2012; p. 465, ISBN 978-1-4419-9598-8.
45. Hollenberg, G.; Gordon, R. Origin of Anomalously High Activation Energies in Sintering and Creep of Impure Refractory. *J. Am. Ceram. Soc.* **1973**, *56*, 109–110. [[CrossRef](#)]
46. Afanasiev, P. Preparation of Mixed Phosphates in Molten Alkali Metal Nitrates. *Chem. Mater.* **1999**, *11*, 1999–2007. [[CrossRef](#)]
47. Tang, Q.Y.; Kan, Y.M.; Wang, P.L.; Li, Y.G.; Zhang, G.J. Nd/V Co-Doped  $\text{Bi}_4\text{Ti}_3\text{O}_{12}$  Powder Prepared by Molten Salt Synthesis. *J. Am. Ceram. Soc.* **2007**, *90*, 3353–3356. [[CrossRef](#)]
48. Chiang, Y.; Birnie, D.; Kingery, W. Chapter 5, Microstructure. In *Physical Ceramics*; J. Wiley & Sons: New York, NY, USA, 1997; p. 354, ISBN 0-471-59873-9.

